Advances in Science and Technology
Research Journal

Advances in Science and Technology Research Journal, 2026, 20(7), 157–175
https://doi.org/10.12913/22998624/218946
ISSN 2299-8624, License CC-BY 4.0

Received: 2026.02.21
Accepted: 2026.05.15
Published: 2026.06.01

Sensitivity analysis of hybrid finite element method/smoothed particle hydrodynamics numerical models for impact loads on sandwich composites

Maciej Robert Roszak[1*], Piotr Kotowski[1]

[1] Department of Mechanics, Materials and Biomedical Engineering, Wrocław University of Science and Technology, Smoluchowskiego 25, 50-370 Wrocław, Poland
* Corresponding author e-mail: maciej.roszak@pwr.edu.pl

ABSTRACT

In this paper, the impact resistance of multilayer sandwich composites was investigated. The outer layers of the composites were made of 1 mm thick 7075 aluminum plates, while the interior consisted of para-aramid fabric in a laminate with a thermoplastic polymer matrix. Three panel variants were prepared: one with a single inner layer of para-aramid fabric, one with six layers, and one with eight layers. During ballistic tests, the samples were shot with 9 × 19 mm Parabellum FMJ and 5.56 × 45 mm FMJ M193 ammunition with initial velocities of 350 ± 10 m/s for the 9×19 mm projectile and 770 ± 10 m/s for the 5.56 × 45 mm projectile, in accordance with the CEN EN 1522 standard. A two-step homogenization method was used to evaluate the material behavior, based on the average laminate results from quasi-static tensile tests, which were then supplemented and compared with the fiber-volume-fraction measurements obtained via optical microscopy. Then, numerical simulations were carried out in the ABAQUS/Explicit dynamic analysis environment using a hybrid FEM/SPH approach. An inverse calibration method was used to preserve the material dynamic behavior. The single-layer sample was fully penetrated by the 9 × 19 mm projectile, whereas the panels containing six and eight layers were not fully penetrated by the 9 × 19 mm projectile, but were completely perforated by the 5.56 × 45 mm M193 round. Comparable results were obtained in the numerical analyses, indicating satisfactory reproduction within the ABAQUS/Explicit simulations. Particular attention was devoted to analyzing the influence of damage parameters – failure displacement and conversion strain – on the residual velocities, as well as on the shape and dimension of material damage for the selected composite configurations. The study contributes to the development of simplified modeling methods for multilayer composites and their calibration in ballistic impact analyses.

Keywords: multilayer ballistic composites, ballistic impact, impact loads, FEM simulations.

INTRODUCTION

Multi-layer composites are commonly used in ballistic shields, not only to reduce the stiffness of the armor, but also to reduce its weight in relation to single-layer vests. Each type of material used to produce the fibers provides them with a specific longitudinal modulus and specific strength. In terms of ballistic shields production, aramid fibers are among the most commonly used types of fibers, which come in varied forms and trade names due to their grammage per m^2. Aramid fibers are also lightweight – 5 times lighter than steel and exhibit high fire resistance, which makes them well-suited for the fabrication of ballistic shields and protective gear [1–3]. These factors greatly influence the mechanical properties and overall behavior of the material when subjected to impact load. During creation of aramid-based composites, the fibers are held together by a matrix, which also contributes to the properties of the material. Matrix allows for higher dissipation of impact energy through cracking. Literature sources show that energy losses due to fracturing can reach up to 35% [4,5].

In recent years, the development of lightweight ballistic protection systems has become a key research direction in military engineering [6,7]. Modern protection concepts increasingly rely on layered steel-composite or ceramic-composite architectures combining high-hardness materials with aramid and ultra-high-molecular-weight polyethylene (UHMWPE) laminates to achieve improved ballistic resistance at reduced areal density [8]. Such configurations are widely applied in light armored vehicles, spall liners, modular protective panels, helmet structures, and soft armor inserts. Recent studies have demonstrated that optimized multilayer composite systems can effectively balance energy absorption, structural integrity, and weight reduction, highlighting the need for experimentally validated and computationally efficient modeling approaches to support their design and optimization [9].

The development of computational methods has enabled the detailed representation of dynamic processes across various fields, including ballistics and disaster engineering [10–12]. This advancement makes it possible to perform the simulations that yield results closely reflecting real-world behavior, thereby supporting the use of numerical tools and advanced computational techniques for optimizing ballistic solutions [13,14]. Such capabilities are particularly valuable given that experimental studies in this area are inherently destructive. Consequently, numerous samples must be manufactured and subjected to destructive testing. From the perspective of developing new solutions, this approach is challenging, as it requires substantial financial resources and often relies on trial-and-error procedures. In this context, simulation-based research becomes highly advantageous, facilitating the design process and enabling the preliminary verification of proposed solutions [15–18].

There are numerous methods used to reproduce the behavior of materials employed in ballistic shields. These approaches are primarily based on constitutive models and, depending on the adopted geometric modeling strategy, they offer varying levels of accuracy. In fiber-level modeling, certain methods focus on representing individual fibers. Such woven structures may be constructed using volumetric elements [18–22] or membrane and shell elements [1,22–25]. This approach is highly effective, as it enables simultaneous consideration of the fabric weave and factors such as friction between individual fibers and yarn layers. However, it is also the most computationally and geometrically demanding method [18,19], particularly when dealing with multilayered or large-scale samples. As the authors emphasize, full 3D modeling is approximately 100 times longer than the variants containing 1D elements, approximately 4 times longer than 2D and 3 times longer than homogenized variants [19,20,22]. Furthermore, modeling fibers in this manner requires a substantial number of finite elements. Another approach involves representing fabrics using representative volume cells (RVC) [13,26–29]. While this method no longer accounts for friction between yarns, it does allow the interface between fibers and warp to be included. From the perspective of computational cost and simulation time, the development of simplified modeling strategies is especially important, as they enable significantly faster simulations and reduce the effort required to prepare numerical models. Such simplified approaches greatly accelerate both the modeling process and the geometric complexity of the model. The most common among them are homogenization techniques and multicontinuum methods [30–32]. These approaches are considerably less computationally intensive and complex than the previously mentioned fiber-level methods.

This study aimed to present a simplified simulation method based on a two-step homogenized multicontinuum approach previously developed by the authors [33–35]. The method is motivated by the need to efficiently bridge the transition between micro-, meso-, and macroscale descriptions of composite materials. At the microscale, individual fibers and matrix regions must be represented explicitly, accounting for local interactions and material heterogeneity. At the mesoscale, yarn architecture, weave patterns, and layer arrangements become essential. At the macroscale, the composite structure is treated as an effective continuous medium. Fully resolving all three scales in a single numerical model is computationally prohibitive, as it requires extremely fine meshes, high memory usage, and long simulation times, especially in dynamic problems such as ballistic impacts. Consequently, simplified or homogenized approaches are necessary to reduce computational cost while preserving the essential mechanical behavior. The proposed method enables a simplified estimation of the volume fractions of fibers and matrix, significantly accelerating the preparation of numerical models without requiring direct modification or explicit reconstruction of the material system. This makes it possible to efficiently analyze large or multi-layered structures while maintaining sufficient predictive accuracy for ballistic applications.

A distinctive aspect of the present study is the use of a thermoplastic matrix based on dicyclopentadiene (DCPD) resin. This material has not yet been extensively examined in multilayer ballistic systems, despite its high toughness, energy-absorption capacity, and advantageous processing characteristics. Another practical contribution is the modular design concept of the composite panels, which allows in the future for multiple units to be combined to achieve higher ballistic resistance classes without redesigning the entire system.

MATERIALS AND METHODS

The experimental part involved the preparation of the composite consisting of para-aramid fabrics embedded in a modified DCPD (dicyclopentadiene) matrix and sandwiched between two aluminum face sheets. After the fabrication of the samples, the field tests were conducted using 9 × 19 mm Parabellum FMJ (full metal jacket) ammunition with an initial velocity of 350 ± 10 m/s and 5.56 × 45 mm FMJ M193 ammunition with an initial velocity of 770 ± 10 m/s. Following the experimental tests, numerical analyses were performed using a modeling approach based on layer homogenization.

Preparation of samples

Each sample was prepared using two aluminum sheets, each 1 mm thick, which served as the outer layers of the composite. The inner part consisted of Twaron® para-aramid fabric with a basis weight of 280 g/m². The fabric had a thickness of 0.4 mm, a fiber density of 1.44 g/cm³, and a fiber diameter of 12 µm. A plain weave architecture was used. The matrix material was a modified DCPD resin, whose preparation procedure and properties are described in detail in [35].

Three types of samples were fabricated. The first type consisted of two outer aluminum layers and a single inner layer of DCPD-impregnated para-aramid fabric. In the second type, the single fabric layer was replaced with six DCPD-impregnated fabric layers, while the third type contained eight such layers, with both configurations retaining the two aluminum face sheets. A schematic diagram of the sample fabrication process is shown in Figure 1.

Ballistic tests

The samples were subjected to field tests using 9 × 19 mm Parabellum FMJ and 5.56 × 45 mm FMJ M193 in accordance with the CEN EN 1522 standard. The experiments were conducted using a weapon dedicated to a given caliber. Each fabricated panel type was fired at with 9 × 19 mm Parabellum FMJ with initial velocity of 350 ± 10 m/s. The 8-layered plate sample was additionally shot with 5.56×45 mm FMJ M193 with initial velocity of 770 ± 10 m/s. In each case, the samples were shot 3 times in different locations. The velocity of the projectiles throughout their flight was measured using Doppler radar integrated with the barrel. The penetration of the shield was recorded using a Phantom VEO 710L high-speed camera at 22,000 frames per second. The recordings were captured at a resolution of 640 × 480 pixels with an exposure time of 5 µs. Using the measured initial velocity of the projectiles, their residual velocity after passing through the sample was calculated, enabling an estimation of the energy absorbed by the material. A scheme of the ballistic testing setup is shown in Figure 2.

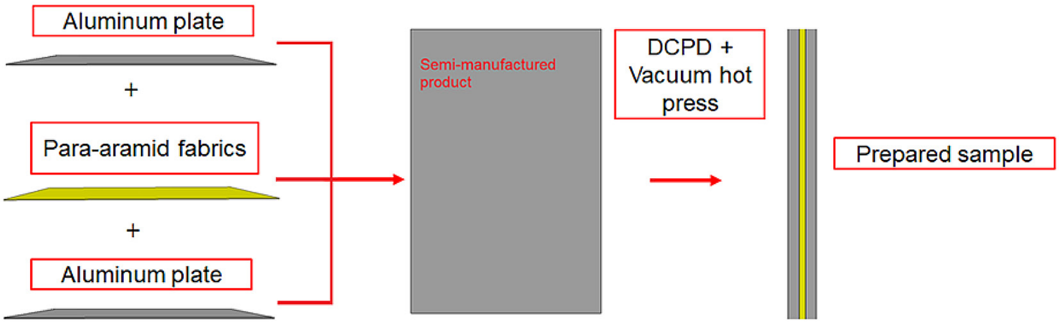

Figure 1. Scheme of the sample preparation procedure

(a) (b)

Figure 2. View of the ballistic tests setup during shooting: (a) shooting position, (b) sample position with high-speed recording camera

Quasi-static tensile tests

A total of five rectangular specimens of para-aramid composite were prepared, each measuring 150 × 20 mm with a uniform thickness of 0.4 mm. The samples were cut from single sheets of fibers embedded in DCPD resin, taken from ready-made samples using a laser plotter, selected for its high dimensional accuracy and minimal thermal influence on the polymer structure. This cutting method ensured smooth, defect-free edges, which is essential to prevent stress concentrations during tensile loading.

Quasi-static tensile tests were conducted using an MTS 793 Bionix universal testing machine (Figure 3). At the start of each test, the initial grip-to-grip distance was set to 100 mm, corresponding to the gauge length. The specimens were clamped symmetrically to ensure a uniform force distribution along the loading axis and to minimize bending effects.

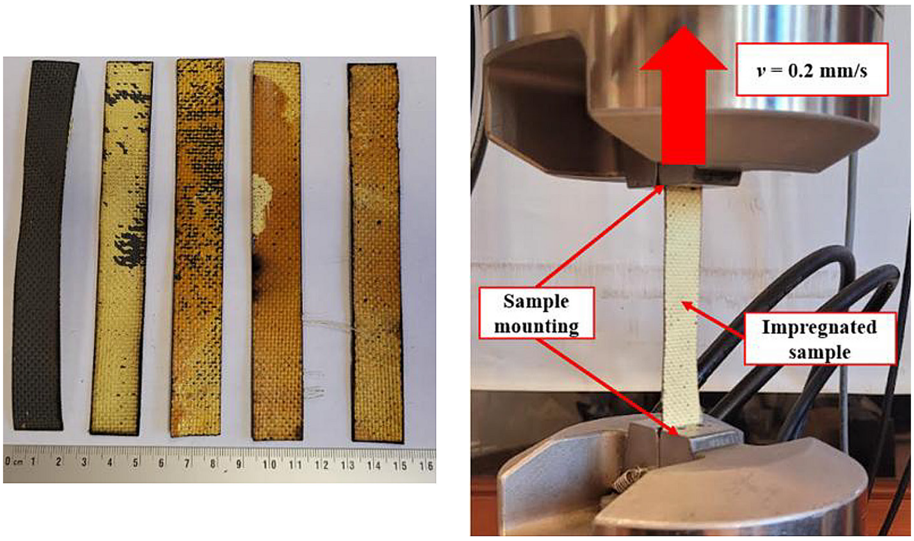

(a) **(b)**

Figure 3. Quasi-static tensile tests: (a) set of prepared samples; (b) a single specimen clamped in the testing machine

All tests were performed at room temperature under a constant crosshead displacement rate of 0.2 mm/s. Each specimen was subjected to tensile loading until complete failure. Throughout the tests, force and displacement were continuously recorded, allowing determination of the stress-strain relationship. Figure 3 shows the prepared specimens and their placement in the testing machine.

Microscopic observations and the homogenization process

Microscopic examinations were performed using a HITACHI TM-3000 scanning electron microscope (SEM) equipped with an EDS/EDX (energy dispersive spectroscopy) detector. The specimens were taken from ten different locations, after which microscopic observations were performed to distinguish between the matrix and the fibers in 10 different areas. Subsequently, histograms were generated using the GIMP software to determine the relative proportions of fibers and matrix in the analyzed areas. Representative images from this process are shown in Figure 4. The images were acquired in secondary electron (SE) mode at an accelerating voltage of 15 kV. The adopted methodology was based on a two-stage homogenization process. The first stage of homogenization involved microscopic examination of the specimen cross-sections to determine the volume fraction of fibers and matrix. Subsequently, a quasi-static tensile test was conducted to verify the assumptions derived from the microscopic observations. The averaged mechanical parameters obtained in this manner were then used in numerical analyses. On the basis of the conducted microscopic observations, the fiber content within the matrix was estimated to be 63%. The estimation was obtained using a color histogram analysis of cross-sectional images, performed at ten different locations on the sample to ensure statistical reliability.

Preparation of numerical models

The Johnson-Cook constitutive strength (1) and damage (2) model was used to describe the metallic components of both the projectiles and the shield. This model accounts for strain rate effects, material hardening under plastic deformation, and thermal softening at high temperatures [36–39].

$$\sigma_y = \left(A + B\underline{\varepsilon}^{p^{n}}\right)(1 + Cln\dot{\varepsilon}^*)(1 - T^{*m}) \quad (1)$$

where: σ_y – true stress [MPa], A – yield strength [MPa], B – strengthening constant [MPa], C – strain rate constant [–], n – strengthening exponent [–], m – thermal softening coefficient [–], $\underline{\varepsilon}^p$ – effective plastic strain [–], $\dot{\varepsilon}^*$ – effective strain rate [–], T^* – homologous temperature [–].

$$\varepsilon_f = [d_1 + d_2 e^{d_3\sigma^*}][1 + d_4 ln\dot{\varepsilon}^*][1 + d_5 T^*] \quad (2)$$

where: e_f – fracture strain [–], $d_1 - d_5$ – failure parameters obtained experimentally [–], σ^* – stress triaxiality factor [–].

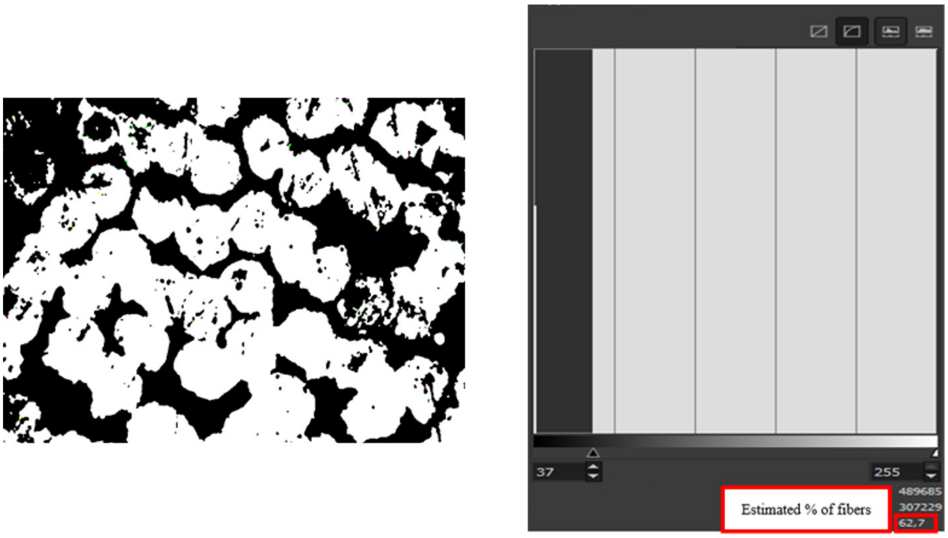

(a) (b)

Figure 4. The procedure of estimating the matrix and the fiber percentage: (a) an example fragment of a sample with enhanced contrast, (b) example color histogram

The material parameters of the projectile metallic components were based on the literature and as well as material properties of aluminum are shown in the tables (Tables 1 and 2, respectively).

The dimensions and component parts of the projectiles were based on real projectiles. The numerical models of the 9 × 19 mm Parabellum FMJ and 5.56 × 45 mm FMJ M193 projectile are presented below (Figure 5, Figure 6). It is important to note that for impacts with the 9 × 19 mm projectile, no additional projectile failure criteria were applied. In contrast, for the high-velocity impact with the M193 projectile, a failure criterion for the lead core was introduced at 100% strain to prevent excessive distortion. Projectile models are available in the supplementary materials as .ipt files.

Orthotropic materials possess mechanical properties that differ along three perpendicular directions, making them ideal for advanced engineering applications such as fiber-reinforced composites [22,34,42,43]. Anisotropy is mathematically represented by a compliance matrix containing three Young's moduli, three shear moduli, and three Poisson's ratios for the orthogonal planes (3).

Table 1. Material parameters for metallic components of projectile [13]

Material	*E* [GPa]	*v* [-]	*ρ* [kg/m^3]	*A* [MPa]	*B* [MPa]	*n* [-]
Lead	13	0.42	11300	35	46	0.48
Brass	130	0.38	8941	112	505	0.42

Table 2. Material parameters for aluminum layer [40,41]

J-C strength model							
Material	*E* [GPa]	*v* [-]	*ρ* [kg/m^3]	*A* [MPa]	*B* [MPa]	*n* [-]	*C* [-]
Al	70	0.3	2700	324	113	0.42	0.002
J-C damage model							
Material	d_1 [-]	d_2 [-]	d_3 [-]	damage evolution [mm]			
Al	-0.77	1.45	-0.47		0.5		

(a) (b)

Figure 5. 9 × 19 mm Parabellum FMJ: (a) numerical model in Abaqus; (b) projectile jacket after discretization with 0.5 mm HEX elements

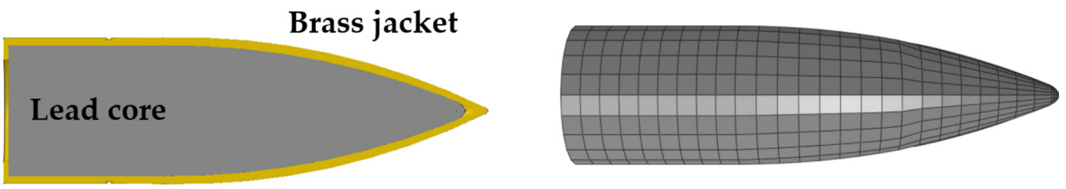

(a) (b)

Figure 6. 5.56 × 45 mm FMJ M193: (a) numerical model in Abaqus; (b) projectile core after discretization with 1 mm HEX elements (to fulfill CFL criterion)

$$\begin{Bmatrix} \varepsilon_{11} \\ \varepsilon_{22} \\ \varepsilon_{33} \\ \gamma_{12} \\ \gamma_{13} \\ \gamma_{23} \end{Bmatrix} = \begin{bmatrix} \frac{1}{E_1} & \frac{-v_{21}}{E_2} & \frac{-v_{31}}{E_3} & 0 & 0 & 0 \\ \frac{-v_{12}}{E_1} & \frac{1}{E_2} & \frac{-v_{32}}{E_3} & 0 & 0 & 0 \\ \frac{-v_{13}}{E_1} & \frac{-v_{23}}{E_2} & \frac{1}{E_3} & 0 & 0 & 0 \\ 0 & 0 & 0 & \frac{1}{G_{12}} & 0 & 0 \\ 0 & 0 & 0 & 0 & \frac{1}{G_{13}} & 0 \\ 0 & 0 & 0 & 0 & 0 & \frac{1}{G_{23}} \end{bmatrix} \begin{Bmatrix} \sigma_{11} \\ \sigma_{22} \\ \sigma_{33} \\ \sigma_{12} \\ \sigma_{13} \\ \sigma_{23} \end{Bmatrix} \tag{3}$$

In the case of woven fabrics, where the weave directions coincide with the principal coordinate axes, the relationships between material parameters can be established as presented below (4).

$$\begin{aligned} E_1 &= E_2 \\ v_{13} &= v_{23} \\ G_{13} &= G_{23} \end{aligned} \tag{4}$$

On the basis of the relationships above, the baseline values used in the numerical analyses were adopted according to (3) and (4), as a layered fabric modeling approach was used. The initial values, along with the values after final calibration, are presented in Table 3.

The final values of the homogenized layers, based on the percentage content of the matrix and fibers, are presented in Table 4. For the static analysis of the homogenized composite, a baseline strain value of 0.045 was adopted, representing only the elastic range of the aramid. In the subsequent part of the study, this value was increased to the range of 0.055-0.065. The increased critical strain reflects dynamic fiber straightening and strain-rate effects, which are not captured in quasi-static calibration.

Similar values after homogenization were also achieved in other works [33,34]. The numerical simulations of the quasi-static tensile test were performed in accordance with the experimental procedure. The finite element model was created based on the specimen dimensions specified in the previous sections, while the initial and boundary conditions replicated the actual clamping configuration used during testing. A mesh sensitivity analysis was conducted using four different element sizes: 0.75, 0.50, and 0.35 mm. The numerical model of the tensile specimen is shown below.

The samples were tested in three variants, with mesh discretizations of 0.35 mm, 0.5 mm, and 0.75 mm in the projectile impact zone (Figure 7). The aim of the analysis was to assess the influence of mesh size and the specified failure criteria values on the simulation results. The side surfaces of the samples were fixed, and the

Table 3. Parameters of materials before homogenization [14,44,45]

Basic parameters of materials before homogenization					
Material	*E* [GPa]	*v* [–]	*ρ* [kg/m³]	*G* [GPa]	*FS* [–]
DCPD	3.1	0.2	98	0.70	0.02
Twaron®	105.0	0.3	1440	3.60	0.08

Table 4. Materials' parameters after homogenization

Parameters of materials after homogenization						
Material	$E_1 = E_2$ [GPa]	E_3 [GPa]	*ρ* [kg/m³]	*v* [-]	*G* [GPa]	*FS* [-]
Fiber-matrix layer	65.0	7.8	1150	0.27	2.30	0.045–0.065* (inversely calibrated)

Note: *E* – Young's moduli in different directions, *ρ* – density, *v* – Poisson's ratio, *G* – shear moduli, *FS* – failure strain.

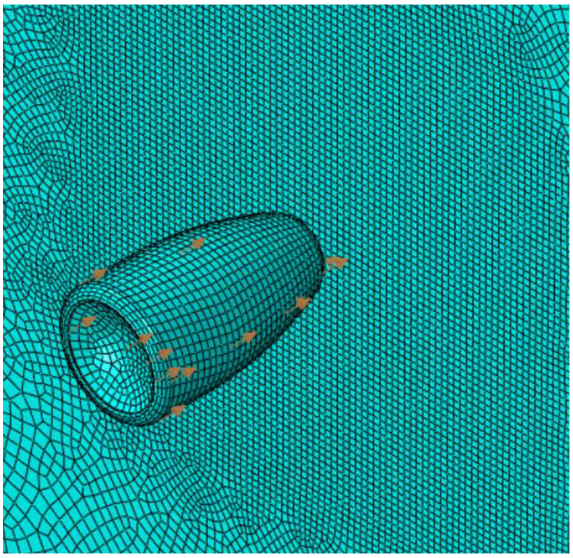

Figure 7. Close-up of the point of contact between the model and the projectile – finite element mesh at the 0.5 mm impact point

friction coefficient was set to 0.2 based on the values reported in the literature [1,23,35]. The stable time increment was set to the default value determined automatically by Abaqus/Explicit, and the total simulation time was 2 × 10^{-4} s for Parabellum projectile and 5 × 10^{-5} s for M193 projectile. No additional mass scaling was applied.

RESULTS

The results of the field testing of the fabricated samples, along with a comparison of the obtained data with finite element method (FEM) simulations, are presented below.

Results of quasi-static tensile tests

The force-displacement curves obtained for the specimens cut from the aramid laminate with a DCPD matrix are shown in Figure 8.

The obtained force-displacement curves exhibit a stable behavior, typical of aramid fabrics. Three characteristic regions can be distinguished in the curves: an initial phase of slow fiber straightening (pre-crimp), the main linear-elastic response of the fibers, and a short plasticization segment just before failure. To derive the stress-strain curves for comparison with the numerical model, the initial pre-crimp region was removed and its displacement was corrected for initial stresses. This procedure ensured that only the elastic range was analyzed.

Microscopic analysis indicated a geometric fiber volume fraction of approximately 63% in the single-layer cross-section. In woven fabrics, only a part of the nominal cross-section is effectively engaged in axial load transfer due to yarn interlacing and crimp. During the initial tensile stage, fiber straightening reduces the effective load-bearing area. To account for these architectural effects, an effective load-bearing thickness equal to 50% of the nominal layer thickness was introduced (0.2 mm for a sample thickness). Using this effective fraction yields a Young's modulus consistent with both homogenization results and literature data, supporting the physical validity of this assumption. A comparison of the curves obtained from homogenization, quasi-static testing, and numerical modeling is presented in Figure 9.

The comparison between the experimentally obtained reduced stress-strain curves and

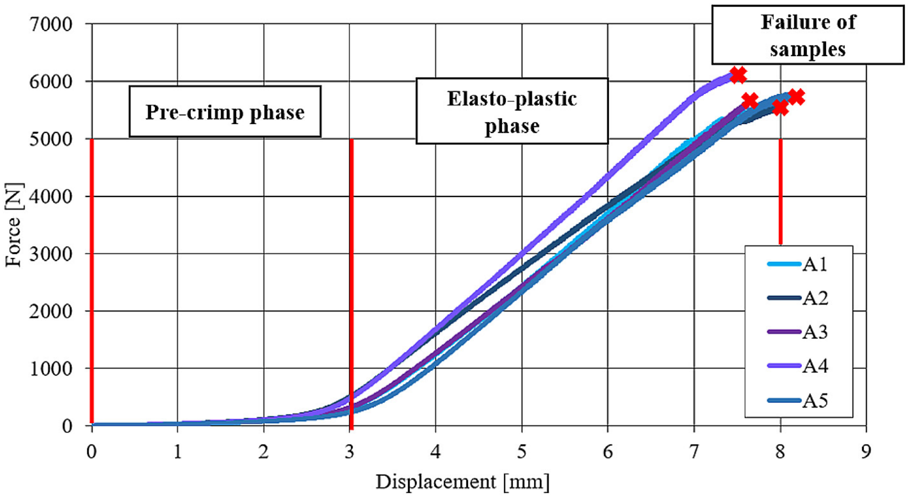

Figure 8. Force-displacement curves for the prepared aramid laminate specimens

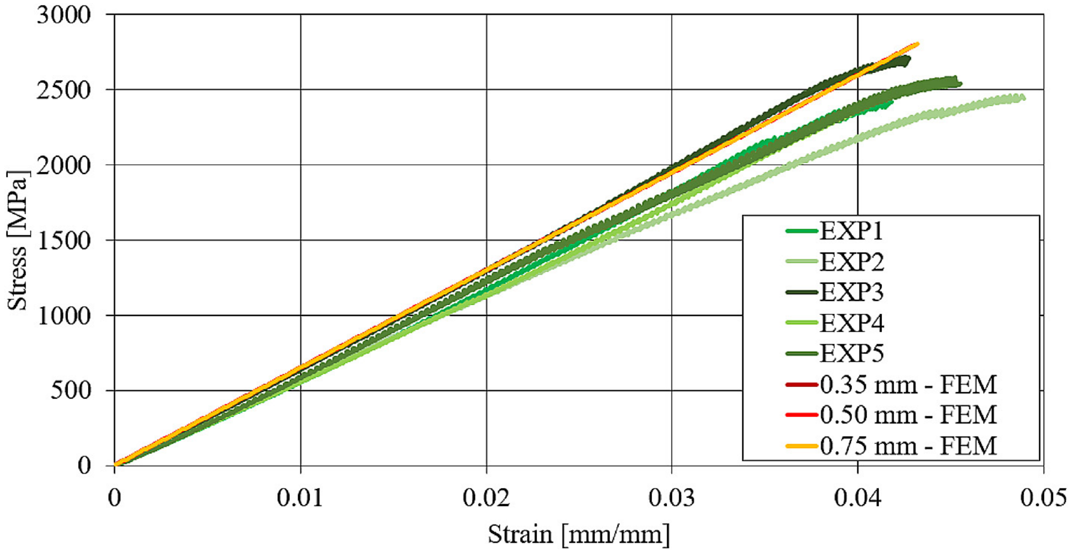

Figure 9. Reduced stress-strain curves for experiments and numerical analysis

the numerical results demonstrates a very good agreement in the elastic range, with the FEM curves (0.35–0.75 mm element sizes).

Minor deviations between the experimental and numerical curves occur in the transition region preceding failure, which is expected due to local fiber waviness, inter-yarn interactions, and microstructural imperfections that are not fully captured by the homogenized elasto-orthotropic model.

Results of ballistic tests

The effects of the ballistic tests are shown in Figures 10–12. In terms of damage observation - for the samples shot with 9 × 19 mm Parabellum FMJ, complete penetration occurred only in the 1-layered sample. For 5.56 × 45 mm FMJ M193, the only tested sample (8-layered) exhibited complete material penetration. The overall effect of

Table 5. The behavior of selected samples as a result of shooting

Projectile	1 layer	6 layers	8 layers
9 × 19 mm Parabellum FMJ	CP	NP	NP
5.56 × 45 mm FMJ M193	(–)	(–)	CP

Note: CP – complete perforation, NP – the projectile was stopped by sample, (–) – the test was not performed.

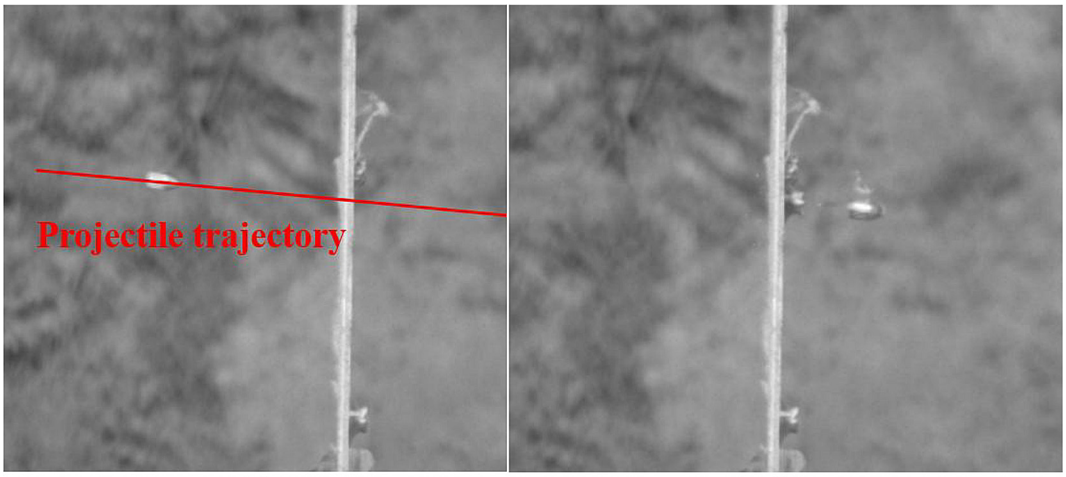

(a) **(b)**

Figure 10. Impact of a 9 × 19 mm Parabellum bullet on a 1-layered sample: (a) projectile trajectory recorded with a high-speed camera; (b) moment of sample perforation, used to determine the residual velocity

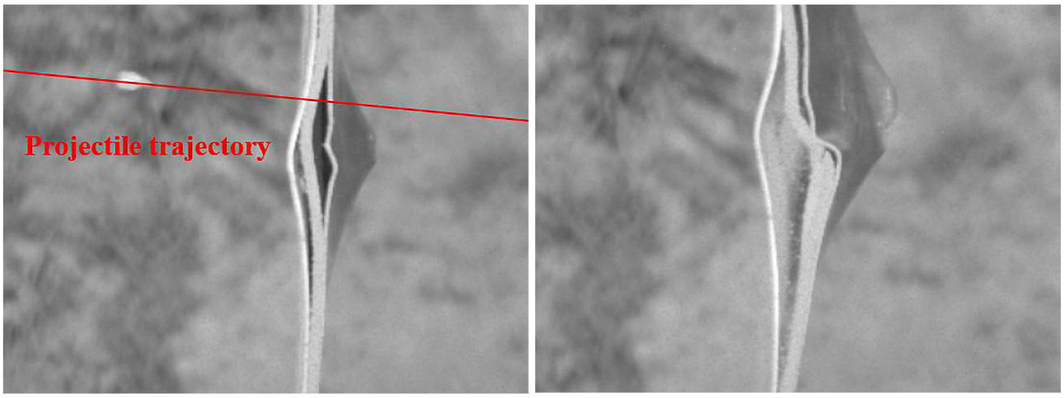

(a) (b)

Figure 11. Impact of a 9 × 19 mm Parabellum bullet on a 6-layered sample: (a) projectile trajectory recorded with a high-speed camera; (b) moment of impact

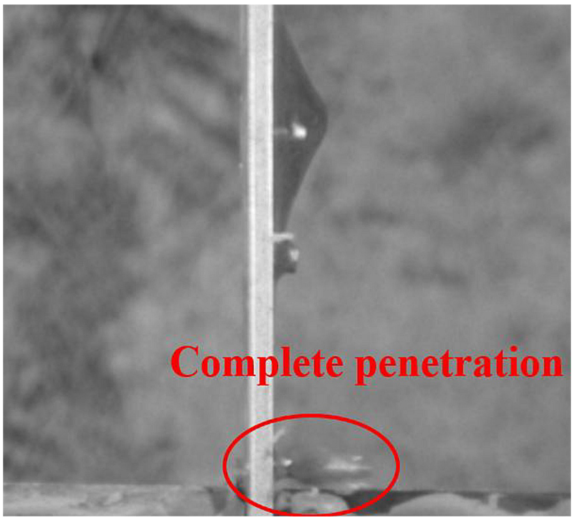

Figure 12. Complete penetration of a 5.56 × 45 mm FMJ M193 bullet through 8-layered sample

the tests performed is presented in the Table 5. The nominal muzzle velocity of the M193 projectile is approximately 990 m/s according to manufacturer's data. However, due to the shorter barrel length and the specific ammunition used in the tests, the impact velocity measured by the high-speed camera at 5–10 m from the muzzle was about 770 m/s, which was adopted as the reference value in the numerical analysis.

Two complete perforations were observed for the single-layer and the 8-layer samples. Owing to side-view recordings using a high-speed camera, it was possible to determine the residual velocities after the projectiles perforated the samples. High-velocity impacts on thin aramid laminates result in a predominance of localized shear plugging with limited energy absorption.

Experimental values are reported as mean ± standard deviation (SD). The coefficient of variation (CV) confirms good repeatability of the measurements. The 95% confidence intervals (CI) were calculated using Student's t-distribution (Table 6).

Results of numerical simulations

The first case analyzed in the numerical simulations involved an impact with a 9 × 19 mm Parabellum projectile. Both the visual impact effect and the resulting entry and exit craters, crater height, as well as the residual velocity after perforation were compared. The assumed value of critical strain was 0.057, while the total stiffness loss of the metallic material was set to 0.5 mm.

Table 6. Statistical summary of experimental ballistic measurements

Configuration	Shots	Parameter	Mean ± SD	CV [%]	95% CI
1-layer	3	Crater height [mm]	13.21 ± 0.34	2.57	13.21 ± 0.84
		Residual velocity [m/s]	323 ± 7	2.17	323 ± 17.4
6-layers		Plastic deflection [mm]	12.50 ± 0.21	1.68	12.50 ± 0.52
8-layers		Crater height [mm]	6.73 ± 0.11	1.63	6.73 ± 0.27
		Residual velocity [m/s]	721 ± 5	0.69	721 ± 12.4

Note: SD – standard deviation, CV – coefficient of variation, CI – confidence interval.

Below (Figure 13, Table 7), a general simulation result is presented for selected finite element mesh dimensions. The following criteria were adopted for evaluating all numerical simulations [46]:

1. Very good correlation with an error: Δe < 10%.
2. Satisfactory correlation with an error: Δe = 11–25%.
3. Significant divergence with an error: Δe = 26–40%.
4. No correlation with an error: Δe > 41%.

The simulation results for the homogenized 1-layered variant indicate that the best correlation in terms of crater height, shape, and residual velocity was obtained for the mesh sizes of 0.35 mm and 0.50 mm in the impact zone, with discrepancies below 10% in both cases. The case with a mesh size of 0.75 mm performed worst in terms of crater height and visual appearance, showing significant divergence, although this was not noticeable for the residual velocity. The next step involved a multi-stage verification of the results for the 6-layered sample. The verification was carried out by comparing the number of damaged layers, sample deflection, and the overall effect of the simulation (Figure 14, Table 8). The projectile shape, which underwent significant plastic deformation, was also compared (Figure 15, Table 9).

The numerical analyses revealed a significant influence of mesh discretization on the obtained results. For the largest mesh size and the initial critical strain value, satisfactory results were achieved for both projectile deflection and the plastic deformation of the shield. Satisfactory results for the smaller mesh sizes were obtained only at a failure strain of 0.065.

The final case analyzed involved the simulations for the 8-layered sample, which was tested with a 5.56 × 45 mm FMJ M193 projectile. Similar to the 1-layered sample, the impacts were fully penetrating, and model verification was performed by comparing the average crater height, the visual crater shape, and the residual

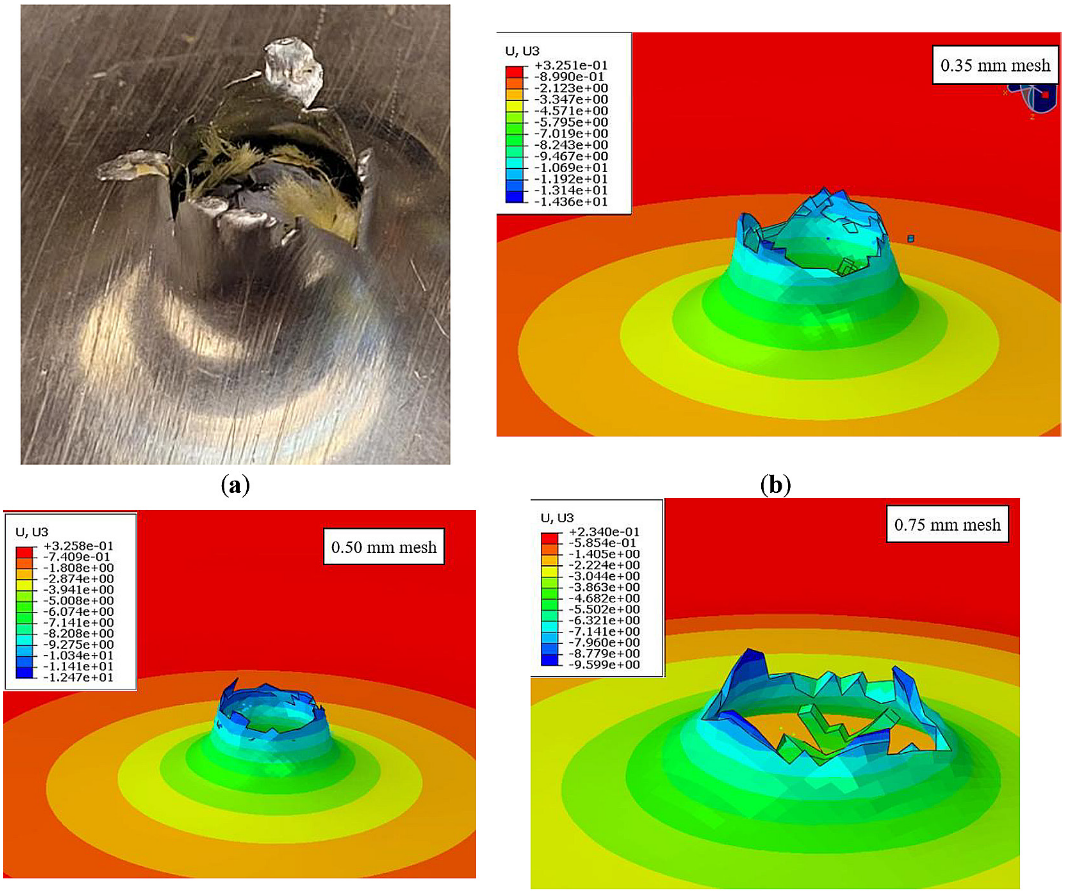

(a) (b)

(c) (d)

Figure 13. Results of numerical simulations: (a) experiment; (b) numerical simulation with mesh size of 0.35 mm; (c) numerical simulation with mesh size of 0.50 mm; (d) numerical simulation with mesh size of 0.75 mm. Time of simulation 1×10^{-4} [s]; dimensions in [mm]

Table 7. Comparison of obtained results for 1-layered sample

Case	Crater height [mm]	Error [%]	Residual velocity [m/s]	Error [%]
Experiment	13.21±0.34	-	323±7	-
0.35 mm mesh	14.36	8.71	311	3.71
0.50 mm mesh	12.47	5.61	311	3.71
0.75 mm mesh	9.59	27.40	312	3.41

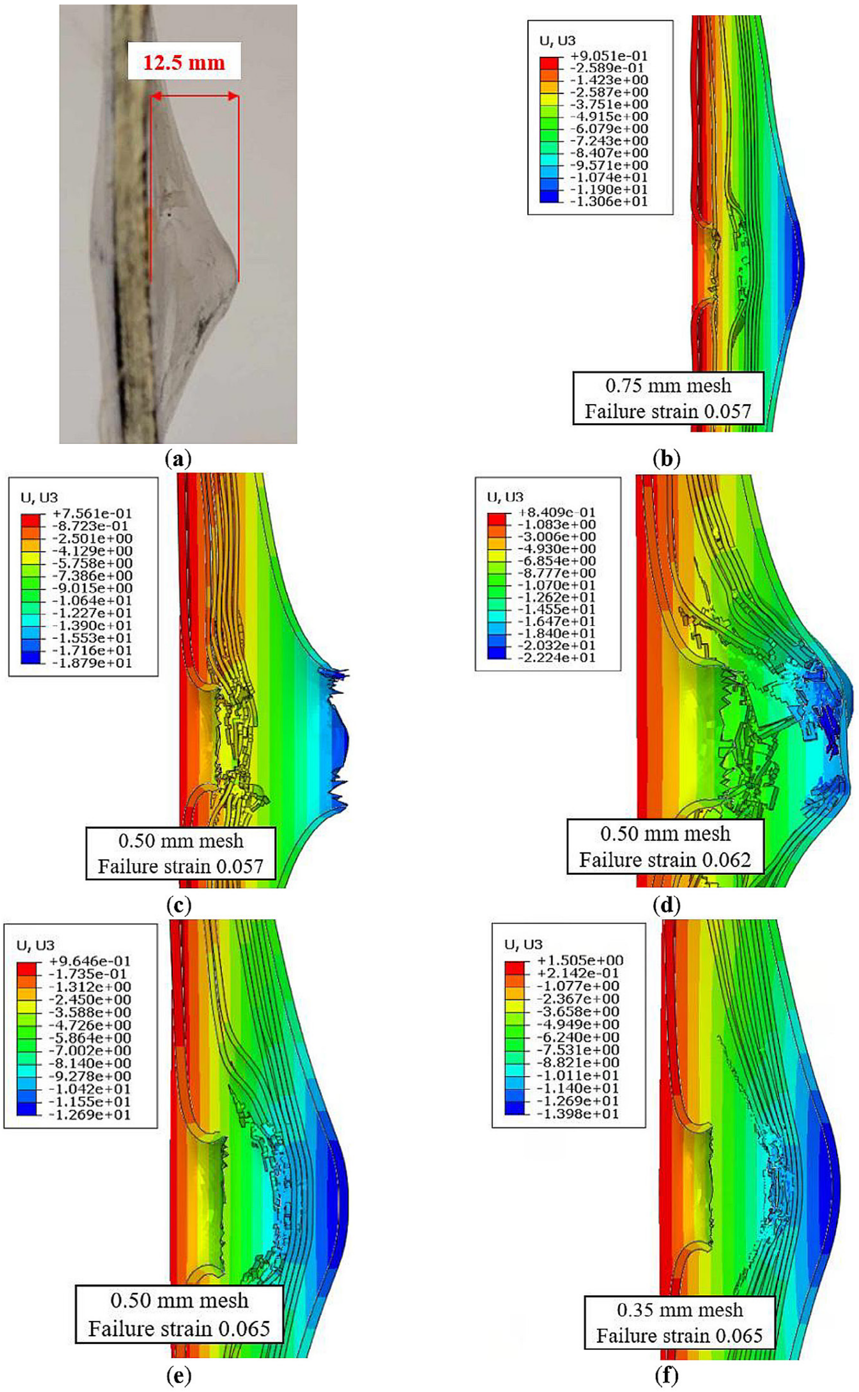

Figure 14. Results of numerical simulations for 6-layered sample: (a) experiment; (b) numerical simulation with mesh size of 0.75 mm, strain limit 0.057; (c) numerical simulation with mesh size of 0.50 mm, strain limit 0.057; (d) numerical simulation with mesh size of 0.50 mm, strain limit 0.062; (e) numerical simulation with mesh size of 0.50 mm, strain limit 0.065; (f) numerical simulation with mesh size of 0.35 mm, strain limit 0.065. Time of simulation 2 × 10^{-4} [s]; dimensions in [mm]

Table 8. Comparison of the obtained results for the 6-layered sample (9 × 19 mm projectile)

Case	Overall effect	Plastic deflection [mm]	Error [%]
Experiment	NP	12.50±0.21	-
0.35 mm mesh – strain limit 0.065	NP	13.98	11.84
0.50 mm mesh – strain limit 0.065	NP	12.69	1.52
0.50 mm mesh – strain limit 0.062	NP	18.79	50.32
0.50 mm mesh – strain limit 0.057	CP	-	-
0.75 mm mesh – strain limit 0.057	NP	13.06	4.48

Note: CP – complete penetration, NP – no penetration.

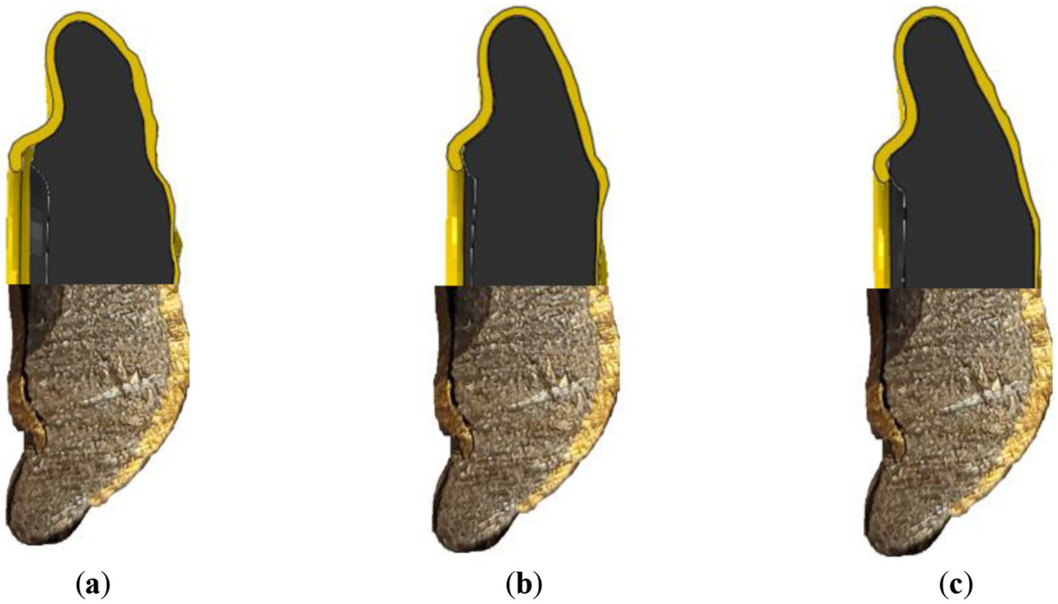

Figure 15. Results of projectile deformation: (a) 0.75 mm mesh sample; (b) 0.50 mm mesh sample; (**c**) 0.35 mm mesh sample

Table 9. Comparison of projectile length and diameter for 6-layered sample

Case	Length [mm]	Error [%]	Diameter [mm]	Error [%]
Experiment	5.99±0.07	-	16.90±0.10	-
0.35 mm mesh	5.34	10.85	17.68	4.62
0.50 mm mesh	5.20	13.19	17.45	2.66
0.75 mm mesh	5.87	2.00	17.16	1.54

velocity at 10 different nodes after perforation (Table 10, Figure 16).

The erosion-based variant led to rapid element removal at the projectile tip, resulting in a sharper and less regular perforation crater with a lower height. The 0.75 mm mesh provided the highest stability in velocity evolution, while the 0.35 mm mesh better captured the crater geometry and the local damage pattern. Overall, the best results were obtained for the 0.35 mm mesh, with acceptable differences in residual velocities and crater characteristics most closely matching the experimental observations.

Numerical energy-distribution plots for representative impact cases are provided in the Supplementary Materials (Figure S1–S3). These plots present the time evolution of the projectile kinetic energy, internal energy of the composite panel, and total system energy. The purpose of this analysis is to demonstrate numerical stability and energy consistency of the hybrid FEM/SPH formulation.

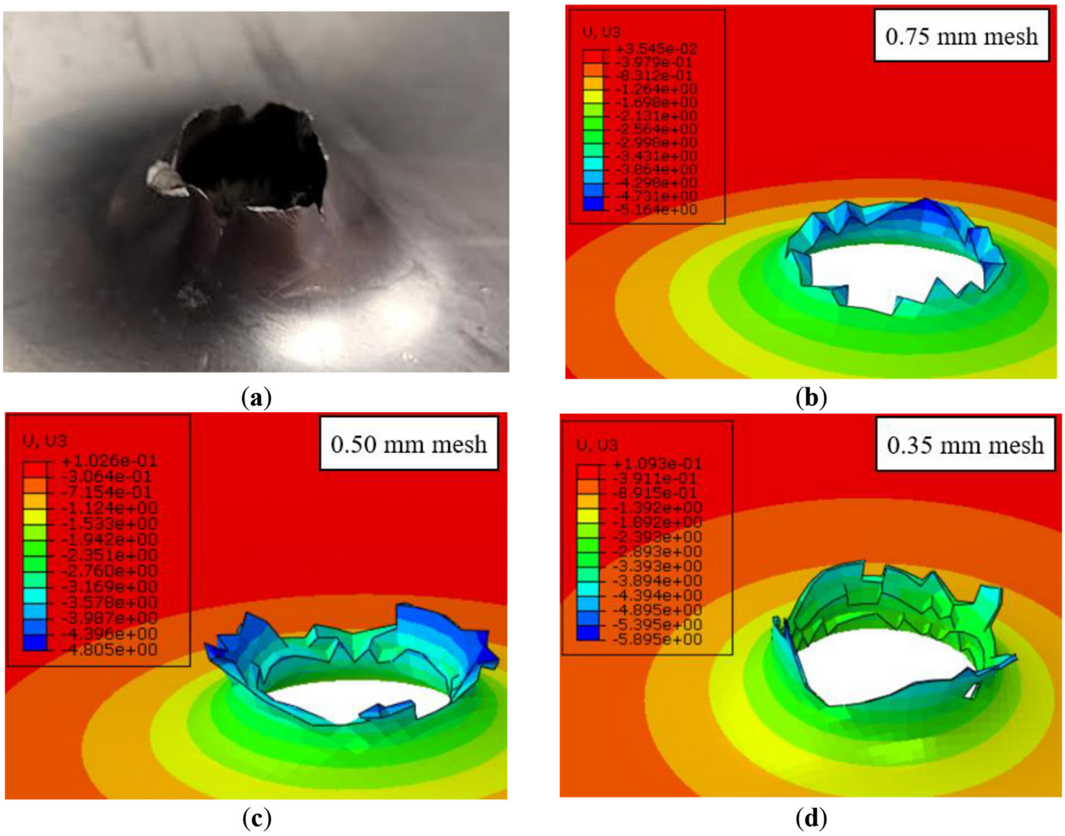

Figure 16. Results of numerical simulations for 8-layered sample: (a) experiment; (b) numerical simulation with mesh size of 0.75 mm; (c) numerical simulation with mesh size of 0.50 mm; (d) numerical simulation with mesh size of 0.35 mm. Time of simulation 4.5×10^{-5} [s]; dimensions in [mm]

Table 10. Comparison of obtained results for 8-layered sample

Case	Crater height [mm]	Error [%]	Residual velocity [m/s]	Error [%]
Experiment	6.73±0.11	-	721±5	-
0.35 mm mesh	5.90	12.33	743	3.05
0.50 mm mesh	4.81	28.53	741	2.77
0.75 mm mesh	5.16	23.32	730	1.25

DISCUSSION

The following section provides a comparison of the calculation methods used and the results obtained in comparison to the available literature.

Ballistic performance against 9 × 19 mm Parabellum

The experimental results for 9 × 19 mm FMJ indicate a clear influence of the number of aramid layers on ballistic resistance. The single-layer sample was fully perforated, whereas both the six-layer and eight-layer configurations prevented complete penetration. This behavior is consistent with the expected scaling of energy absorption in thin aramid laminates, where progressive failure involves fiber stretching, delamination, and limited shear plugging, as also reported in [1,4,32,47,48].

The measured residual velocity for the single-layer panel (323 ± 7 m/s) and the absence of perforation for the thicker variants align with the earlier findings for Twaron-based laminates of comparable areal density. Sen et al. [1] and Pach et al. [32] reported that the laminates below approximately 3–4 mm thickness typically fail through localized shear plugging under 9 × 19 mm impacts, with minimal ability to disperse load in-plane. The same mechanism was observed in the present study, confirmed by high-speed imaging and crater morphology.

For the six- and eight-layer samples, the absence of perforation suggests that the combination of two aluminum sheets and multilayer aramid core effectively stabilized the target and increased load distribution capability. Similar behavior was reported for hybrid metal-aramid structures in [49,50], where aluminum face sheets reduced local deformation and delayed laminate rupture.

Although both thick samples resisted penetration, the six-layer sample showed only two destroyed layers, indicating that for thin metal-aramid sandwiches the damage depth does not scale linearly with the number of layers. This result agrees with the nonlinear damage progression described in [5,24,51], where the initial layers absorb a disproportionately larger share of impact energy.

Comparison of numerical model performance with literature

To identify the most efficient discretization strategy, two additional performance metrics were introduced: the geometric error index (5) and the velocity error index (6). The aggregated error as a function of element size is presented in Figure 17, enabling identification of the discretization range.

$$GEI(h) = \frac{1}{N}\sum_{i=1}^{N}\left|\frac{V_{num}(h) - V_{exp}}{V_{exp}}\right| \cdot 100\% \quad (5)$$

$$VEI(h) = \frac{1}{N}\sum_{i=1}^{N}\left|\frac{H_{num}(h) - H_{exp}}{H_{exp}}\right| \cdot 100\% \quad (6)$$

where: h – finite element size [mm], N – number of tests, V – residual velocity obtained in simulations and experiments [m/s], H – crater height obtained in simulations and experiments [mm].

Such levels of correlation fall within the typical ranges presented by validated woven-fabric models in earlier studies. Chocron et al. [23] and Wisniewski and Gmitrzuk [14] reported that homogenized models of Twaron fabrics reproduce experimental energy absorption within 5–15% error, depending on element size and strain-rate treatment. Similarly, the multiscale approaches described by Nilakantan et al. [30] and Carvelli and Poggi [31] showed that simplified RVC-based or continuum models, when properly calibrated, can effectively capture the macroscopic stiffness and failure behavior of woven composites.

The results also highlight the strong influence of mesh density and failure strain on the stability of dynamic simulations. Similar observations were noted in [22,32,52], particularly for thin laminates exposed to high strain-rate loading. A comparison of the results obtained in this work with other available works is presented in Table 11.

Limitations of present work

The adopted strain-based failure formulation represents a local damage model and does not include a characteristic length scale. Consequently, the onset of element erosion remains

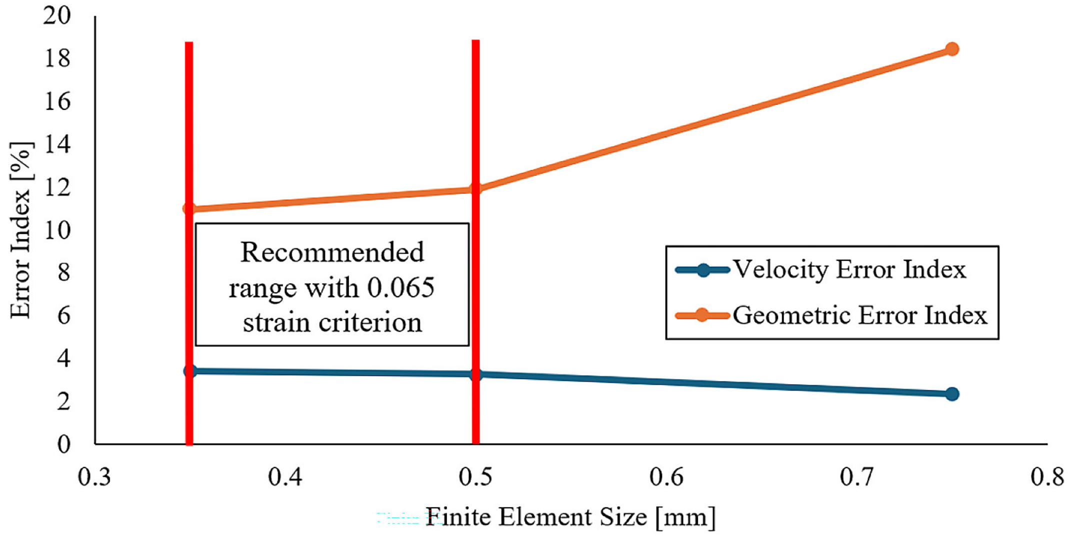

Figure 17. Comparison of the velocity error index (VEI) and geometric crater index (GCI) as a function of element size

Table 11. Comparison of numerical models results for pistol ammunition with data from the literature

Reference	Numerical approach	Material system	Typical agreement with experiments	Comparison with the present numerical model (9 × 19 mm)
Sen et al. (2019) [1]	Homogenized STF-Kevlar layers, explicit FE model	Kevlar + shear-thickening fluid	5–12% error in residual velocity, good perforation prediction	The present model yields residual velocity errors of 3–4% and crater-height deviations below 10%, remaining within the ranges reported in the literature
Pach et al. (2017) [32]	Orthotropic laminate model	Polymer composite laminates	5–15% error in residual velocity, moderate agreement in deformation	The present model demonstrates residual-velocity errors of 3–4% with satisfactory reproduction of crater geometry
Pyka et al. (2019) [53]	Abaqus/Explicit model for 9 × 19 mm impact	Thermoplastic laminate	3–10% error in residual velocity, minor crater shape differences	Comparable residual-velocity agreement, with consistent crater-height prediction for refined mesh sizes (0.35–0.50 mm)
Chocron et al. (2010) [23]	Homogenized multi-layer woven fabric	Aramid woven fabric	5–15% energy-error range, correct damage sequence	The present results reflect a similar failure progression and fall within the geometric error ranges reported for pistol-velocity impacts
Scazzosi et al. 2018 [19]	Homogenized orthotropic laminate with the full 2D Chang-Chang failure criterion	Panel made of plain weave Kevlar® 29	Residual velocity reproduced with approx. 17% error for macro and 11% for meso	The results obtained in this study show comparable levels of agreement, although the laminate configuration differs in layering scheme

mesh-dependent. Although a systematic mesh-sensitivity analysis and inverse calibration of the critical strain were performed to mitigate this effect, full discretization objectivity cannot be guaranteed. Future work may incorporate nonlocal damage formulations or crack-band regularization techniques to improve mesh objectivity and transferability of calibrated parameters. The performed global error assessment, presented in Figure 17, partially mitigates this limitation by identifying the discretization range in which the numerical response remains stable. The homogenized representation of the aramid-matrix layer does not explicitly account for yarn-level friction, crimp evolution, inter-yarn sliding, or progressive delamination mechanisms. These microstructural effects may influence local damage development under high strain-rate loading and are only indirectly represented within the present continuum framework. Future developments may incorporate surrogate modeling techniques, such as Kriging-based metamodels, to enable uncertainty quantification and reliability-driven optimization [54].

CONCLUSIONS

On the basis of the conducted experimental investigations and numerical simulations using the proposed two-step homogenization strategy, the following conclusions can be drawn:

- The applied strain-based failure criterion exhibits pronounced mesh sensitivity due to the absence of an internal characteristic length. The most stable and accurate results were obtained for element sizes of 0.35–0.50 mm in the impact zone, where crater height errors remained below 10% and residual velocity errors below 4%.
- The calibrated critical strain range of 0.055–0.065 enabled satisfactory agreement between experimental and numerical results for multilayer configurations, particularly for the 6-layer specimen. Reduction of the finite element size from 0.75 mm to 0.35 mm required an increase of the calibrated critical fracture strain by approximately 20% in order to maintain agreement with experimental observations.
- The single-layer configuration was fully perforated by the 9 × 19 mm projectile, with a measured residual velocity of 323 ± 7 m/s, whereas both 6- and 8-layer panels prevented penetration under the same loading conditions.
- The 5.56 × 45 mm FMJ M193 projectile fully perforated the 8-layer panel, confirming the limitations of thin metal-aramid sandwich systems against rifle-level threats.
- The proposed homogenized modeling approach provides a computationally efficient alternative to detailed fiber-level modeling with an error margin below 5% in selected cases.

Acknowledgments

The authors would like to thank Mr. Grzegorz Skrzypczak and Mr. Dariusz Pyka for assistance in conducting the ballistics tests. Calculations were carried out at the Wroclaw Centre for Networking and Supercomputing (http://www.wcss.pl (accessed on 1–30 November 2025)), grant no. 452.

REFERENCES

1. Sen S, Jamal M N Bin, Shaw A, Deb A. Numerical investigation of ballistic performance of shear thickening fluid (STF)-Kevlar composite. Int J Mech Sci 2019;164. https://doi.org/10.1016/J.IJMECSCI.2019.105174
2. Hu Q ran, Shen X yu, Qian X ming, Huang G yan, Yuan M qi. The personal protective equipment (PPE) based on individual combat: A systematic review and trend analysis. Defence Technology 2023;28:195–221. https://doi.org/10.1016/J.DT.2022.12.007
3. Zhai Y, Mao L, Shen Y, Yan X. Research progress of cut-resistant textile materials. Front Chem 2021;9:745467. https://doi.org/10.3389/FCHEM.2021.745467/BIBTEX
4. Iannucci L, Dechaene R, Willows M, Degrieck J. A failure model for the analysis of thin woven glass composite structures under impact loadings. Comput Struct 2001;79:785–99. https://doi.org/10.1016/S0045-7949(00)00190-5
5. Zee RH, Hsieh CY. Energy loss partitioning during ballistic impact of polymer composites. Polym Compos 1993;14:265–71. https://doi.org/10.1002/PC.750140312
6. Sun Q, Lin J, Gai Y, Li Y. Ballistic performance of the UHMWPE fiber-reinforced composite helmet: Experiments and numerical simulations. Thin-Walled Structures 2025;210:113037. https://doi.org/10.1016/j.tws.2025.113037
7. Lin J, Li Y, Liu S, Fan H. Numerical investigation of the high-velocity impact performance of body armor panels. Thin-Walled Structures 2023;189:110909. https://doi.org/10.1016/j.tws.2023.110909
8. Viliš J, Kosiuczenko K, Nowakowski M, Tupaj M, Trytek A, Zouhar J, et al. Comprehensive evaluation of layered composite protection performance for light armored vehicles. Journal of Materials Engineering and Performance 2025;34:28643–60. https://doi.org/10.1007/s11665-025-11553-3
9. Birhan M, Negash B, Batu T, Abunu Y. Integrating composite materials throughout the military sector: A review. Advances in Materials Science and Engineering 2026;2026. https://doi.org/10.1155/amse/9931653
10. Wdowicz D, Ptak M. numerical approaches to pedestrian impact simulation with human body models: A review. Archives of Computational Methods in Engineering 2023;30:4687–709. https://doi.org/10.1007/S11831-023-09949-2
11. Baranowski P, Małachowski J, Mazurkiewicz Ł. Local blast wave interaction with tire structure. Defence Technology 2020;16:520–9. https://doi.org/10.1016/J.DT.2019.07.021
12. Kucewicz M, Baranowski P, Mazurkiewicz Ł, Małachowski J. Comparison of selected blasting constitutive models for reproducing the dynamic fragmentation of rock. Int J Impact Eng 2023;173:104484. https://doi.org/10.1016/J.IJIMPENG.2022.104484
13. Ziółkowski G, Pach J, Pyka D, Kurzynowski T, Jamroziak K. X-ray computed tomography for the development of ballistic composite. Materials 2020;13:5566. https://doi.org/10.3390/MA13235566
14. Validation of Numerical Model of the Twaron® CT709 Ballistic Fabric n.d. https://promechjournal.pl/article/01.3001.0002.5094/en (accessed October 7, 2025).
15. Moldtmann P, Berk J, Ryan S, Klavzar A, Limido J, Lange C, et al. Adaptive optimisation of explosive reactive armour for protection against kinetic energy and shaped charge threats. Defence Technology 2024;40:1–12. https://doi.org/10.1016/J.DT.2024.05.007
16. Ćwik TK, Iannucci L, Curtis P, Pope D. Design and ballistic performance of hybrid composite laminates. Applied Composite Materials 2016;24:717–33. https://doi.org/10.1007/S10443-016-9536-X
17. Bandaru AK, Ahmad S. Ballistic impact behaviour of thermoplastic Kevlar composites: parametric studies. Procedia Eng 2017;173:355–62. https://doi.org/10.1016/J.PROENG.2016.12.029
18. Titire L, Muntenita C. Ballistic impact study of an aramid fabric by changing the projectile trajectory. Fibers 2025;13:8. https://doi.org/10.3390/FIB13010008
19. Scazzosi R, Manes A, Petrone G, Giglio M. Two different modelling approaches for fabric composites subjected to ballistic impact. IOP Conf Ser Mater Sci Eng 2018;406:012051. https://doi.org/10.1088/1757-899X/406/1/012051
20. Feito N, Loya JA, Muñoz-Sánchez A, Das R. Numerical Modelling of Ballistic Impact Response at Low Velocity in Aramid Fabrics. Materials 2019;12:2087. https://doi.org/10.3390/MA12132087
21. Soni G, Singh R, Mitra M, Falzon BG. Modelling matrix damage and fibre–matrix interfacial decohesion in composite laminates via a multi-fibre multi-layer representative volume element (M2RVE). Int J Solids Struct 2014;51:449–61. https://doi.

org/10.1016/J.IJSOLSTR.2013.10.018

22. Zochowski P, Bajkowski M, Grygoruk R, Magier M, Burian W, Pyka D, et al. Finite element modeling of ballistic inserts containing aramid fabrics under projectile impact conditions – Comparison of methods. Compos Struct 2022;294:115752. https://doi.org/10.1016/J.COMPSTRUCT.2022.115752
23. Chocron S, Figueroa E, King N, Kirchdoerfer T, Nicholls AE, Sagebiel E, et al. Modeling and validation of full fabric targets under ballistic impact. Compos Sci Technol 2010;70:2012–22. https://doi.org/10.1016/J.COMPSCITECH.2010.07.025
24. Das S, Jagan S, Shaw A, Pal A. Determination of inter-yarn friction and its effect on ballistic response of para-aramid woven fabric under low velocity impact. Compos Struct 2015;120:129–40. https://doi.org/10.1016/J.COMPSTRUCT.2014.09.063
25. Xie Z, Chen W, Liu Y, Liu L, Zhao Z, Luo G. Design of the ballistic performance of shear thickening fluid (STF) impregnated Kevlar fabric via numerical simulation. Mater Des 2023;226:111599. https://doi.org/10.1016/J.MATDES.2023.111599
26. Li S, Sitnikova E. Representative volume elements and unit cells: Concepts, Theory, Applications and Implementation 2020:1–468. https://doi.org/10.1016/C2017-0-03559-0
27. Dewangan MK, Panigrahi SK. Finite element analysis of hybrid 3D orthogonal woven composite subjected to ballistic impact with multi-scale modeling. Polym Adv Technol 2021;32:964–79. https://doi.org/10.1002/PAT.5143
28. Dewangan MK, Panigrahi SK. Finite element analysis of projectile nose shapes in ballistic perforation of 2D plain woven Kevlar/epoxy composites using multi-scale modelling. Journal of Industrial Textiles 2022;51:4200S-4230S. https://doi.org/10.1177/1528083720970168
29. Dewangan MK, Panigrahi SK. Multi-scale modeling of three-dimensional angle interlock woven composite subjected to ballistic impact using FEM. Polym Adv Technol 2020;31:3079–94. https://doi.org/10.1002/PAT.5033
30. Nilakantan G, Keefe M, Bogetti TA, Adkinson R, Gillespie JW. On the finite element analysis of woven fabric impact using multiscale modeling techniques. Int J Solids Struct 2010;47:2300–15. https://doi.org/10.1016/J.IJSOLSTR.2010.04.029
31. Carvelli V, Poggi C. A homogenization procedure for the numerical analysis of woven fabric composites. Compos Part A Appl Sci Manuf 2001;32:1425–32. https://doi.org/10.1016/S1359-835X(01)00041-0
32. Pach J, Pyka D, Jamroziak K, Mayer P. The experimental and numerical analysis of the ballistic resistance of polymer composites. Compos B Eng 2017;113:24–30. https://doi.org/10.1016/J.COMPOSITESB.2017.01.006
33. Olaleye K, Jamroziak K, Bocian M. Effect of Core Type on the Ballistic Performance of Aramid Reinforced Composite 2025:814–23. https://doi.org/10.1007/978-3-031-96114-4_84
34. Olaleye K, Pyka D, Kurzawa A, Bocian M, Jamroziak K. Energy absorption behavior of aramid/DCPD backing to determining the blunt trauma criterion of a human head in a ballistic helmet. Compos Struct 2024;340:118172. https://doi.org/10.1016/J.COMPSTRUCT.2024.118172
35. Roszak M, Pyka D, Bocian M, Barsan N, Dragašius E, Jamroziak K. Multi-layer fabric composites combined with non-newtonian shear thickening in ballistic protection—hybrid numerical methods and ballistic tests. Polymers 2023;15:3584. https://doi.org/10.3390/POLYM15173584
36. Wang X, Shi J. Validation of Johnson-Cook plasticity and damage model using impact experiment. Int J Impact Eng 2013;60:67–75. https://doi.org/10.1016/J.IJIMPENG.2013.04.010
37. Zhang H, Hu D, Ye X, Chen X, He Y. A simplified Johnson-Cook model of TC4T for aeroengine foreign object damage prediction. Eng Fract Mech 2022;269:108523. https://doi.org/10.1016/J.ENGFRACMECH.2022.108523
38. Chang L, Yuan S, Huang X, Cai Z. Determination of Johnson-Cook damage model for 7xxx laminated aluminum alloy and simulation application. Mater Today Commun 2023;34:105224. https://doi.org/10.1016/J.MTCOMM.2022.105224
39. Zhang Y, Outeiro JC, Mabrouki T. On the selection of johnson-cook constitutive model parameters for Ti-6Al-4 V using three types of numerical models of orthogonal cutting. Procedia CIRP 2015;31:112–7. https://doi.org/10.1016/J.PROCIR.2015.03.052
40. Roszak M, Pyka D, Stępczak M, Sweklej P, Jambroziak K, Bocian M. Ballistic resistance tests of a fuel tank intended for installation in an armored vehicle. Archive of Mechanical Engineering 2025. https://doi.org/10.24425/AME.2025.155870
41. Spear DG, Palazotto AN, Kemnitz RA. Modeling and simulation techniques used in high strain rate projectile impact. Mathematics 2021;9:274. https://doi.org/10.3390/MATH9030274
42. Zhou Y, Chen X. A numerical investigation into the influence of fabric construction on ballistic performance. Compos B Eng 2015;76:209–17. https://doi.org/10.1016/J.COMPOSITESB.2015.02.008
43. Wang K, Zhou X, Ren W, Wu Y, Yu Y, Zhou Y, et al. The impact of the coupling relationship between projectile size and yarn dimension on the ballistic performance of plain weave fabric. Defence Technology 2025;43:288–303. https://doi.org/10.1016/J.DT.2024.06.016
44. Pyka D, Jamroziak K, Ziolkowski G, Pach J, Bocian M. Research on ballistic resistance of DCPD Laminate Under Pistol Ammunition

Fire. 2018:14–7. 24th International Conference May 14 – 17, 2018, Svratka, Czech Republic. https://doi.org/10.21495/91-8-701

45. Zhu L, Zhu G, Feng J, Jin L, Ma P. Impact tensile behavior analysis of Twaron fiber tows from fast Fourier transform. Textile Research Journal 2019;89:1363–70. https://doi.org/10.1177/0040517518775917
46. Zochowski P, Bajkowski M, Grygoruk R, Magier M, Burian W, Pyka D, et al. Comparison of numerical simulation techniques of ballistic ceramics under projectile impact conditions. Materials 2022, Vol 15, Page 18 2021;15:18. https://doi.org/10.3390/MA15010018
47. Eckhoff D, Thomesen S, Heisserer U, Børvik T. Ballistic response behaviour of Dyneema® HB210 curved armour plates: An experimental and numerical study. Thin-Walled Structures 2025;213:113265. https://doi.org/10.1016/J.TWS.2025.113265
48. Chen L, Cao M, Fang Q. Ballistic performance of ultra-high molecular weight polyethylene laminate with different thickness. Int J Impact Eng 2021;156:103931. https://doi.org/10.1016/J.IJIMPENG.2021.103931
49. Carrillo JG, Gonzalez-Canche NG, Flores-Johnson EA, Cortes P. Low velocity impact response of fibre metal laminates based on aramid fibre reinforced polypropylene. Compos Struct 2019;220:708–16. https://doi.org/10.1016/J.COMPSTRUCT.2019.04.018
50. Gonzalez-Canche NG, Flores-Johnson EA, Carrillo JG. Mechanical characterization of fiber metal laminate based on aramid fiber reinforced polypropylene. Compos Struct 2017;172:259–66. https://doi.org/10.1016/J.COMPSTRUCT.2017.02.100
51. Tabiei A, Ivanov I. Materially and geometrically non-linear woven composite micro-mechanical model with failure for finite element simulations. Int J Non Linear Mech 2004;39:175–88. https://doi.org/10.1016/S0020-7462(02)00067-7
52. Yang EC, Linforth S, Ngo T, Tran P. Hybrid-mesh modelling & validation of woven fabric subjected to medium velocity impact. Int J Mech Sci 2018;144:427–37. https://doi.org/10.1016/J.IJMECSCI.2018.05.017
53. Pyka D, Pach J, Jamroziak K. Numerical modeling of ballistic resistance of thermoplastic laminate under 9 × 19 mm parabellum ammunition. 25th INTERNATIONAL CONFERENCE May 13–16, 2019, Svratka, Czech Republic. https://doi.org/10.21495/71-0-307
54. Luo C, Zhu SP, Keshtegar B, Macek W, Branco R, Meng D. Active Kriging-based conjugate first-order reliability method for highly efficient structural reliability analysis using resample strategy. Comput Methods Appl Mech Eng 2024;423:116863. https://doi.org/10.1016/j.cma.2024.116863